Qubit readout enabled by qubit cloaking

Manuel H. Muñoz-Arias[1,*] Cristóbal Lledó[1,†] and Alexandre Blais[1,2]

[1]*Institut Quantique and Département de Physique, Université de Sherbrooke, Sherbrooke, Quebec J1K 2R1, Canada*

[2]*Canadian Institute for Advanced Research, Toronto, Ontario M5G1M1, Canada*

Time-dependent drives play a crucial role in quantum computing efforts with circuit quantum electrodynamics. They enable single-qubit control and entangling logical operations, as well as qubit readout. However, their presence can lead to deleterious effects such as large ac-Stark shifts and unwanted qubit transitions ultimately reflected into reduced control or readout fidelities. Qubit cloaking was introduced by Lledó *et al.* [C. Lledó, R. Dassonneville, A. Moulinas *et al.*, Nat. Commun. **14**, 6313 (2023)] to temporarily decouple the qubit from the coherent photon population of a driven cavity, allowing for the application of arbitrary displacements to the cavity field while avoiding the deleterious effects on the qubit. For qubit readout, cloaking permits us to prearm the cavity with an, in principle, arbitrarily large number of photons, in anticipation of the qubit-state-dependent evolution of the cavity field, allowing for improved readout strategies. Here, we take a closer look at two such strategies: first, *arm-and-release* readout, introduced together with qubit cloaking, where after arming the cavity, the cloaking mechanism is released and the cavity field evolves under the application of a constant drive amplitude; and, second, an *arm-and-longitudinal* readout scheme, where the cavity drive amplitude is slowly modulated after the release. We show that the two schemes complement each other, offering an improvement over standard dispersive readout for any values of the dispersive interaction and the cavity decay rate, as well as any target measurement integration time. Our results provide a recommendation for improving qubit readout without changes to the standard circuit-QED architecture.

I. INTRODUCTION

Qubit readout is an indispensable operation in quantum information processing [1]. For superconducting qubits, the standard method is dispersive readout, which consists in driving and measuring the response of a cavity the resonant frequency of which is shifted depending on the state of a far-detuned coupled qubit [2,3]. An advantage of dispersive readout is that at small measurement powers, it is close to quantum nondemolition (QND) [4–8]. However, non-QNDness at moderate power results in readout errors that have not yet reached the 10^{-3} level for measurement times of the order of 100 ns [9–12], lagging behind the best-performance numbers of single-qubit and entangling gates [13–16]. Improving dispersive readout further is crucial to reach fault tolerance in the circuit-QED architecture for applications such as quantum error correction [17–20].

In principle, increasing the strength of the cavity drive, leading to a larger cavity photon population, can lead to improved readout [2]. However, this is not an ideal solution, as even a modest photon population can result

in unwanted qubit transitions, including leakage out of the computational subspace of the transmon [4,8,21–23]. Cavity drives also cause an ac-Stark frequency shift of the qubit and broadening of the qubit line width via measurement-induced dephasing [24–27]. Recently, an alternative approach to accelerating and improving the fidelity of dispersive readout has been demonstrated [7]. It is based on adding a cloaking drive on the qubit, which allows the cavity to be armed with photons in a qubit-state-unconditional way. During the arming phase, the qubit is oblivious to the coherent state in the cavity, thereby not experiencing ac-Stark shifts or measurement-induced dephasing. Once the desired mean photon population is reached, the cloaking mechanism can be released, allowing the cavity field to evolve in a qubit-state-dependent way as in standard dispersive readout. In this paper, we explore how this additional control—the armed photon population—allows for optimizations of the phase-space trajectories of the cavity to maximize readout fidelity at short integration times.

One readout strategy where phase-space trajectories of the cavity field maximally distinguish the ground and excited states of the qubit at short measurement times is longitudinal readout [28]. It relies on a qubit-resonator

---

*munm2002@usherbrooke.ca
†cristobal.lledo.veloso@usherbrooke.ca

coupling between the qubit σ^z and one of the resonator quadrature operators (e.g., the P quadrature) with a modulated coupling frequency g_z. This interaction produces a cavity-field displacement in opposite directions in phase space when the qubit is in the ground or excited state. While longitudinal interaction has been physically implemented in circuit QED [29,30], modulation of the coupling frequency has remained challenging, with no experimental demonstration so far of longitudinal readout except in its synthetic versions [6,31].

Building upon the arm-and-release idea, in this work we introduce a protocol for synthesizing a longitudinal-readout process after the release step. The intuition is that the positions of the fixed point of the average cavity field—$\alpha_{g,e}^s$ for the (g)round or (e)xcited qubit state—can be pushed or pulled by slowly modulating the drive amplitude, tailoring the trajectories followed by the time-dependent amplitudes $\alpha_{g,e}(t)$. This can be arranged in such a way that $\alpha_g(t)$ and $\alpha_e(t)$ separate from each other in exactly opposite directions in phase space, as under the longitudinal interaction, something we refer to as arm-and-longitudinal readout. This is illustrated in Fig. 1, which shows the path in phase space of the cavity-pointer states for dispersive readout (dashed lines), the arm-and-release approach (dash-dotted lines), and the arm-and-longitudinal protocol (full lines). Crucially, this *arm-and-longitudinal* readout protocol is only possible due to qubit cloaking [7], as the cavity needs to start from an *armed* state with nonzero field amplitude. To account for and avoid ionization [4,21–23], it proves convenient that, under this modulation, the amplitudes $|\alpha_{g,e}(t)|$ increase monotonously in time until they reach a chosen maximum value, which can be taken to be below the ionization threshold.

In this paper, we show that either arm-and-release or arm-and-longitudinal always outperforms standard dispersive readout for any measurement time and any ratio χ/κ of the dispersive interaction χ and the cavity decay rate κ. In particular, we show that for signal integration times $\gtrsim 10/\kappa$, the arm-and-longitudinal protocol outperforms the other two. These results can inform the design and manipulation of current and future superconducting qubit devices. Moreover, while we focus on circuit QED with superconducting qubits, these results are general and can be used in other platforms.

The rest of this paper is organized as follows. In Sec. II, we briefly remind the reader about standard dispersive readout in the two-level-system approximation and in Sec. III, about qubit cloaking and the *arm-and-release* scheme. In Sec. IV, we explain how to transform arm-and-release into arm-and-longitudinal readout. Having introduced all the main ideas, in Sec. V we provide a performance comparison between the three schemes. In Sec. VI, we show that the arm-and-longitudinal is valid beyond the two-level-system approximation for the transmon, the rotating-wave approximation, and the dispersive
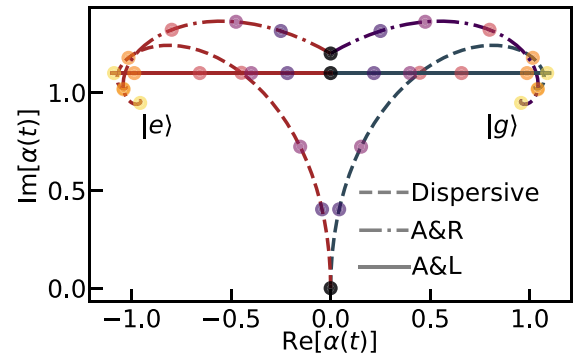

FIG. 1. The path in phase space of the cavity amplitude when the qubit is in the ground (blue) or excited (red) state for the three different schemes: dispersive readout (dashed line), arm-and-release (A&R, dashed-dotted line), and arm-and-longitudinal (A&L, full line). The colored dots indicate different times in the evolution, $\kappa t = 0, 1, 2, 4, 10$, and 20. The parameters are as follows: $|\chi|/\kappa = 1$ and $\varepsilon_1/2\pi = 19.85$ MHz and 18.49 MHz as well as $\alpha_{\text{arm}}/\sqrt{n_{\text{max}}} \approx 0.8$ and $1/\sqrt{2}$ for arm-and-release and arm-and-longitudinal, respectively.

approximation. Finally, in Sec. VII, we discuss our results and offer an outlook.

II. BRIEF ON DISPERSIVE QUBIT READOUT

We start by giving a short introduction to dispersive qubit readout in the two-level-system approximation [2]. The Jaynes-Cummings Hamiltonian ($\hbar = 1$)

$$\hat{H}_{\text{JC}} = \omega_r \hat{a}^\dagger \hat{a} + \frac{\omega_q}{2}\hat{\sigma}^z + g_c(\hat{\sigma}^+ \hat{a} + \hat{\sigma}^- \hat{a}^\dagger) \quad (1)$$

describes the interaction between a qubit and a cavity mode in the rotating-wave approximation. Here, $\hat{a}$ is the annihilation operator of the cavity mode of fundamental frequency ω_r, $\hat{\sigma}^{z,+,-}$ are, respectively, the Pauli-z, raising, and lowering operators for the qubit of fundamental frequency ω_q, and g_c is the interaction frequency. In the dispersive regime, where $|\omega_q - \omega_r| \gg g_c$, the Hamiltonian is approximately diagonalized, up to second order in $g_c/|\omega_q - \omega_r|$, as

$$\hat{U}^\dagger \hat{H}_{\text{JC}} \hat{U} \approx \hat{H}_{\text{disp}} = \left(\omega_r + \frac{\chi}{2}\hat{\sigma}^z\right)\hat{a}^\dagger \hat{a} + \frac{\tilde{\omega}_q}{2}\hat{\sigma}^z, \quad (2)$$

where $\chi = 2g_c^2/(\omega_q - \omega_r)$ is the (full) dispersive interaction, $\tilde{\omega}_q = \omega_q + \chi/2$ is the Lamb-shifted qubit frequency, and $\hat{U} = \exp\{[g_c/(\omega_q - \omega_r)](\hat{a}^\dagger \hat{\sigma}^- - \hat{a}\hat{\sigma}^+)\}$.

As the arrangement of the interaction term in Eq. (2) suggests, here we adopt the convention that the cavity frequency is pulled by $-\chi/2$ if the qubit is in the ground state $|g\rangle$ and by $+\chi/2$ if it is in the excited state $|e\rangle$. As a result, by measuring the response of the cavity to an external drive, one can infer the state of the qubit. For

example, an initial condition $(c_g |g\rangle + c_e |e\rangle) |0\rangle$ evolves to $c_g |g, \alpha_g\rangle + c_e |e, \alpha_e\rangle$ under the combined action of Eq. (2) and the drive

$$\hat{H}_1(t) = -\varepsilon_1(t)(\hat{a} e^{i\omega_1 t} + \text{h.c.})/2, \tag{3}$$

where $|0\rangle$ is the cavity vacuum state and $\alpha_{g,e}$ are coherent-state amplitudes that act as pointer states and evolve as

$$\dot{\alpha}_{g,e} = -[i(\omega_r - \omega_1 \mp \chi/2) + \kappa/2]\alpha_{g,e} + i\varepsilon_1(t)/2 \tag{4}$$

in a frame rotating at the drive frequency ω_1 and where $\varepsilon_1(t)$ is the cavity drive amplitude. Equation (4) is obtained by using the dispersive approximation on the Lindblad master equation [32,33]

$$\partial_t \hat{\rho} = -i[\hat{H}_{\text{JC}} + \hat{H}_1(t), \hat{\rho}] + \kappa \mathcal{D}[\hat{a}]\hat{\rho}, \tag{5}$$

where $\mathcal{D}[\hat{a}]\hat{\rho} \equiv \hat{a}\hat{\rho}\hat{a}^\dagger - (1/2)\{\hat{a}^\dagger \hat{a}, \hat{\rho}\}$. For simplicity, we assume in Eq. (4) that the qubit state remains constant.

III. QUBIT CLOAKING AND ARM-AND-RELEASE READOUT

As introduced in Ref. [7], cloaking a qubit in a cavity allows us to decouple the qubit from the classical part of a cavity field. This approach, which is achieved with an appropriately chosen drive on the qubit, has been shown to lead to faster dispersive readout via an arm-and-release scheme. The latter consists in arming the cavity with photons while cloaking the qubit and subsequently releasing the cloaking mechanism, allowing the dispersive readout dynamics to proceed. Noting from Eq. (4) that the paths of the coherent states $\alpha_{g,e}$ will (for $\omega_1 = \omega_r$) initially separate from one another along the X quadrature at a speed $\text{Re}[\dot{\alpha}_g - \dot{\alpha}_e] \propto \chi \sqrt{\bar{n}(t)}$, where $\bar{n}(t)$ is the mean photon number, the arm-and-release approach has the clear advantage of having a finite initial speed ($\bar{n}(0) \neq 0$) due to the armed photons, unlike in dispersive readout, where $\bar{n}(0) = 0$. Moreover, since high-fidelity qubit gates can be realized on a cloaked qubit, the arming time does not factor into the readout time [7].

The intuition behind the cloaking mechanism is the following. The cavity drive Eq. (3) results in a coherent state inside the cavity, which acts as an effective classical drive on the qubit [23]. An additional drive on the qubit can destructively interfere with this effective drive, leaving the qubit to experience the cavity as if it was in the vacuum state. To make this observation more precise, consider applying a displacement transformation $\hat{a} \rightarrow \hat{a} + \alpha(t)$ on Eq. (5), with $\alpha(t)$ chosen to eliminate the effect of the cavity drive. Due to the qubit-cavity coupling term ($\propto g_c$), this transformation effectively passes the drive to the qubit and the displaced Hamiltonian reads $\hat{H}_{\text{JC}} + g_c(\alpha(t)\hat{\sigma}^+ +$

$\alpha^*(t)\hat{\sigma}^-)$. With an additional qubit cancellation drive

$$\hat{H}_2(t) = -g_c(\alpha(t)\hat{\sigma}^+ + \alpha^*(t)\hat{\sigma}^-), \tag{6}$$

the effective drive on the qubit is cancelled out in the displaced frame, where the Hamiltonian is just the undriven $\hat{H}_{\text{JC}}$ of Eq. (1). Here, the complex amplitude $\alpha(t)$ corresponds to the coherent-state amplitude of the cavity field in the absence of the qubit, namely, it evolves according to $\dot{\alpha}(t) = -(i\omega_r + \kappa/2)\alpha(t) + i\varepsilon_1(t)e^{-i\omega_1 t}/2$ in the laboratory frame. The above results are exact and can be made to account for the rapidly rotating terms that were (implicitly) ignored in Eq. (1), as well as to account for the multilevel nature of superconducting qubits. Moreover, the result remains unchanged if qubit dissipation and dephasing are included [7]. The picture emerging from qubit cloaking is that the cavity field is displaced in phase space by an amount $\alpha(t)$ that is qubit-state independent. Equivalently, the qubit is not affected by this displacement.

Having introduced the fundamentals of qubit cloaking and described the steps involved in arm-and-release readout, we study the expected performance of this approach. Since the arming time does not factor into the readout time, for the rest of this section we assume the intracavity field to start at a chosen position along the P quadrature in phase space. That is, without loss of generality, we take a purely imaginary $\alpha(0) = i\alpha_{\text{arm}}$ with some real and positive α_{arm}. Furthermore, during the release step ($t > 0$), we take the amplitude ε_1 of the cavity drive to remain constant. With these two conditions, we can integrate Eq. (4) to obtain

$$\begin{aligned} \alpha_e(t) = &\; \alpha_{\text{arm}} \left[\sin\left(\frac{\chi t}{2}\right) + i\cos\left(\frac{\chi t}{2}\right) \right] e^{-\frac{\kappa}{2}t} \\ &+ \tilde{\varepsilon}_1 \left\{ \chi - \left[\chi\cos\left(\frac{\chi t}{2}\right) + \kappa\sin\left(\frac{\chi t}{2}\right) \right] e^{-\frac{\kappa}{2}t} \right\} \\ &+ i\tilde{\varepsilon}_1 \left\{ \kappa + \left[\chi\sin\left(\frac{\chi t}{2}\right) - \kappa\cos\left(\frac{\chi t}{2}\right) \right] e^{-\frac{\kappa}{2}t} \right\}, \end{aligned} \tag{7}$$

where $\tilde{\varepsilon}_1 = \varepsilon_1/(\chi^2 + \kappa^2)$ and the expression for $\alpha_g(t)$ is obtained by replacing $\chi \rightarrow -\chi$. We recover the result expected for standard dispersive readout when taking $\alpha_{\text{arm}} \rightarrow 0$ in Eq. (7). By noting that the expressions for $\alpha_e(t)$ and $\alpha_g(t)$ differ only in their real parts, the contribution of the term proportional to α_{arm} to the measurement signal is $\propto \text{Re}[\alpha_g(t) - \alpha_e(t)] = 2\alpha_{\text{arm}} \sin(|\chi| t/2)e^{-\kappa t/2}$. At short times, this contribution is positive, enriching the signal.

For fixed parameters, the amplitudes $\alpha_{g,e}$ reach the same steady states for both dispersive and arm-and-release readout but the maximum mean photon numbers $\bar{n}_{\text{max}}$ visited during the trajectories are not the same (for an explicit expression for $\bar{n}(t)$, see Appendix A). Since qubit ionization sets a maximum mean photon number for quantum

nondemolition readout [22], to make a fair comparison we first choose $(\chi, \kappa, \varepsilon_1)$ for the standard dispersive dynamics and then we adjust ε_1 for arm-and-release such that both schemes share the same $\bar{n}_{\max}$. In Fig. 1, we compare the phase-space trajectories for dispersive readout (dashed lines) and arm-and-release (dashed-dotted lines). While arm-and-release is clearly faster than dispersive readout (see the colored dots), fixing the maximum photon number makes the two fixed points of arm-and-release have a smaller separation than those of dispersive readout. As we will discuss in Sec. V, there is an important trade-off between speed at short times and long-time state discrimination that influences the performance of the different readout schemes.

To compare the performance of the arm-and-release approach to that of dispersive readout, we compute, for both cases, the signal-to-noise ratio (SNR) for homodyne detection of the X quadrature of the cavity output field. The corresponding integrated measurement operator up to time τ is given by $\hat{M}(\tau) = \sqrt{\kappa} \int_0^\tau dt K(t)[\hat{a}_{\text{out}}^\dagger(t) + \hat{a}_{\text{out}}(t)]$ [3,34]. In this expression, $K(t)$ is a filter function and $\hat{a}_{\text{out}}$ represents the output field related to the intracavity field via the input-output boundary condition $\hat{a}_{\text{out}} = \hat{a}_{\text{in}} + \sqrt{\kappa}\hat{a}$, where $\hat{a}_{\text{in}}$ is the input field [35]. The signal is defined as $|\langle \hat{M}(\tau)\rangle_e - \langle \hat{M}(\tau)\rangle_g|$ and the imprecision noise is given by the fluctuations around the mean field of $\hat{M}$, i.e., $\hat{M}_N(\tau) = \hat{M}(\tau) - \langle \hat{M}(\tau)\rangle$. Putting these two elements together, the squared SNR can be expressed as [3]

$$\text{SNR}^2 = \frac{|\langle \hat{M}(\tau)\rangle_e - \langle \hat{M}(\tau)\rangle_g|^2}{\langle \hat{M}_N^2(\tau)\rangle_e + \langle \hat{M}_N^2(\tau)\rangle_g}. \tag{8}$$

The filter $K(t)$ should favorably weight times where the signal is larger; thus, naturally, the optimal filter is $K(t) = |\langle \hat{M}(t)\rangle_e - \langle \hat{M}(t)\rangle_g|$ [34,36]. Assuming that the input and output fields remain coherent and in the limit of unit-efficiency measurement, we obtain [34]

$$\text{SNR}^2 = 2\kappa \int_0^\tau dt \, \text{Re}[\alpha_e(t) - \alpha_g(t)]^2. \tag{9}$$

Even though the full analytical expression of the SNR for arm-and-release is rather long and thus uninformative (see Appendix A), there are some interesting properties that are worth discussing. As pointed out previously, the arm-and-release scheme receives a boost compared to dispersive readout stemming from the nonzero photons in the initial condition. This is manifested in the SNR, the short-time scaling, $\kappa\tau \ll 1$, of which reads

$$\text{SNR}_{\text{A\&R}} \approx \sqrt{\frac{2}{3}}\frac{\alpha_{\text{arm}}|\chi|}{\kappa}(\kappa\tau)^{3/2} \tag{10}$$

and is to be contrasted with the short-time scaling of standard dispersive readout,

$$\text{SNR}_{\text{disp}} \approx \frac{1}{8}\sqrt{\frac{3}{2}}\frac{\varepsilon_1|\chi|}{\kappa^2}(\kappa\tau)^{5/2}. \tag{11}$$

With arm-and-release, we thus acquire signal at a faster rate proportional to α_{arm}. Remarkably, this rate is equal to the rate exhibited by ideal longitudinal qubit readout [28]. We illustrate this in Fig. 2(b) by comparing the SNR as a function of the integration time for the case of $|\chi|/\kappa = 1$, which is optimal for dispersive readout [37]. In the short-measurement-time regime, the different scalings are evident from the slopes of the dashed-dotted line (arm-and-release) and the dashed line (dispersive readout); furthermore, even at $\kappa\tau \to 0$, a clear improvement is observed, corroborating our observation of the enhancement provided by a nonzero α_{arm}.

In the opposite limit of long measurement times, $\kappa\tau \gg 1$, the SNR is dominated by the term

$$\text{SNR}_{\text{A\&R}} \approx \sqrt{8}\frac{\varepsilon_1}{\kappa}\frac{|\chi|/\kappa}{1 + (\chi/\kappa)^2}\sqrt{\kappa\tau}, \tag{12}$$

which is the same long-measurement-time SNR as for dispersive readout. This is because at long times, the contribution coming from α_{arm} has decayed, as is evident from the first line of Eq. (7). As such, in this asymptotic limit, the ratio $|\chi|/\kappa = 1$ corresponds to the optimal working point for both arm-and-release and dispersive readout. To illustrate this, in Figs. 2(b) and 2(c) we show the SNR at different measurement times versus $|\chi|/\kappa$ for dispersive [Fig. 2(b)] and arm-and-release [Fig. 2(c)] readout, respectively. In both cases, the maximum approaches $\chi/\kappa = 1$ at long times. It is also worth noting that for short measurement times, the optimal value of $|\chi|/\kappa$ is > 1 in both cases, with arm-and-release reaching the asymptotic value faster. Moreover, for each of the measurement times used in Figs. 2(b) and 2(c), arm-and-release has a larger maximum SNR than dispersive readout as a consequence of the boost coming from α_{arm}.

IV. ARM-AND-LONGITUDINAL READOUT

As anticipated in Sec. I, arm-and-release readout can be transformed into arm-and-longitudinal readout by the appropriate choice of the time-dependent drive amplitude $\varepsilon_1(t)$. Let us start with the simple intuition behind this scheme. As shown in Fig. 1, the arm-and-release amplitudes $\alpha_{g,e}(t)$ curve toward the real phase-space axis as time increases, moving toward their fixed points $\alpha_{g,e}^s = \varepsilon_1/(\mp\chi - i\kappa)$. To make the coherent amplitudes separate along the X quadrature in a straight line without curving, we slowly increase $\varepsilon_1(t)$ in time so as to push away the fixed points that the trajectories follow.
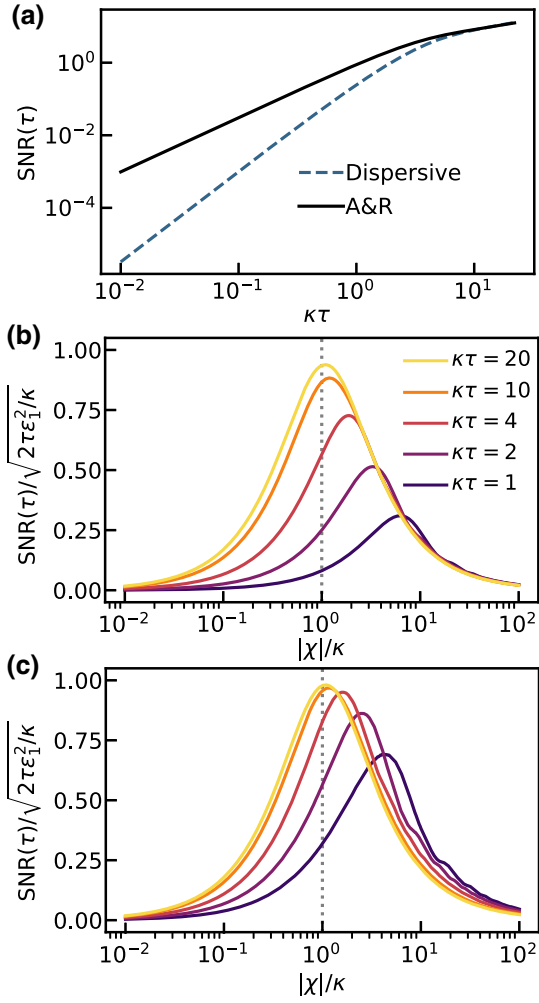
FIG. 2. (a) The signal-to-noise ratio (SNR) as a function of the measurement integration time for dispersive (dashed) and arm-and-release (solid) readout, for the corresponding pairs of trajectories shown in Fig. 1. (b),(c) The normalized SNR versus $|\chi|/\kappa$ for (b) dispersive and (c) arm-and-release readout. The different curves correspond to different measurement integration times in units of $1/\kappa$.

The explicit form of $\varepsilon_1(t)$ needed to obtain longitudinal-like displacements of the cavity field $\alpha_{g,e}(t)$ can be obtained from Eq. (4) by imposing the condition that the displacement is only along the X quadrature ($\omega_r = \omega_1$). With the initial condition $\alpha(0) = i\alpha_{\mathrm{arm}}$, we obtain (see Appendix B)

$$\varepsilon_1(t) = \alpha_{\mathrm{arm}} \frac{\chi^2}{\kappa} \left(1 - e^{-\frac{\kappa}{2}t}\right) + \alpha_{\mathrm{arm}} \kappa. \quad (13)$$

Using this expression, the qubit-state-dependent coherent amplitudes take the desired longitudinal-like motion along the real phase-space axis:

$$\alpha_{g,e}(t) = \mp \alpha_{\mathrm{arm}} \frac{\chi}{\kappa} \left(1 - e^{-\frac{\kappa}{2}t}\right) + i\alpha_{\mathrm{arm}}. \quad (14)$$

This arm-and-longitudinal scheme requires $\alpha_{\mathrm{arm}} \neq 0$ and is thus enabled by our ability to prearm the cavity field using qubit cloaking [7]. We remark that the frequency of the drive needs to be chosen in between the two qubit-state-dependent frequency responses of the cavity ($\omega_r \pm \chi/2$), which is important to ensure that the drive modulation necessary for arm-and-longitudinal is independent of the qubit state.

In Fig. 1, we show the arm-and-longitudinal trajectories in phase space corresponding to Eq. (14) (solid lines), comparing them to the arm-and-release and dispersive readout. For a fair comparison, the three pairs of trajectories visit the same maximum mean photon number. While at short times the coherent amplitudes $\alpha_{g,e}(t)$ separate faster for arm-and-release, at long times the separation is larger for arm-and-longitudinal, hinting at an interesting trade-off between the two schemes. We can anticipate that, depending on the ratio $|\chi|/\kappa$ and the target measurement integration time, one or the other might be the best strategy. We devote Sec. V to this analysis.

Substituting Eq. (14) into Eq. (9), we find, for the SNR of the arm-and-longitudinal readout,

$$\mathrm{SNR}_{\mathrm{A\&L}} = \sqrt{8} \frac{\alpha_{\mathrm{arm}}|\chi|}{\kappa} \sqrt{\kappa\tau - 3 + 4e^{-\frac{\kappa}{2}\tau} - e^{-\kappa\tau}}. \quad (15)$$

At short times $\kappa\tau \ll 1$, this takes the simpler form

$$\mathrm{SNR}_{\mathrm{A\&L}} \approx \sqrt{\frac{2}{3}} \frac{\alpha_{\mathrm{arm}}|\chi|}{\kappa} (\kappa\tau)^{3/2} \quad (16)$$

and thus offers better performance than dispersive readout, the SNR of which is $\propto (\kappa\tau)^{5/2}$ [see Eq. (11)]. We note that the expression in Eq. (15) has the same functional form as the SNR obtained for a modulated longitudinal qubit-cavity interaction [28], the Hamiltonian of which is

$$H_z(t) = i g_z(t) \hat{\sigma}^z (\hat{a}^\dagger - \hat{a}), \quad (17)$$

where $\tilde{g}_z$ is the amplitude of $g_z(t)$, which is modulated at the cavity frequency, provided that we include the optimal filter [38] and identify $\alpha_{\mathrm{arm}}|\chi|$ with $\tilde{g}_z$.

This comparison suggests that, in a prearmed cavity, the product $\alpha_{\mathrm{arm}}|\chi|$ plays the role of an effective interaction driving the readout dynamics. Importantly, realizing the Hamiltonian Eq. (17) requires a qubit-cavity coupling that is different from the standard capacitive coupling of circuit QED, which, rather, leads to Eq. (1) [28,39,40]. In contrast, our arm-and-longitudinal approach can be implemented without changes to the standard circuit-QED architecture [3].

Although arm-and-release and arm-and-longitudinal share the same short-time SNR scaling, the values of the armed amplitude, α_{arm} in Eqs. (10) and (16), are not the same. For fixed values of $|\chi|/\kappa$, measurement time, and

maximum mean photon number $\bar{n}_{\max}$, we can optimize over α_{arm} to maximize the SNR of arm-and-release. On the other hand, for arm-and-longitudinal readout, the value of the initial amplitude α_{arm} is fixed and from Eq. (14) it reads

$$\alpha_{\mathrm{arm}} = \sqrt{\frac{\bar{n}_{\max}}{1 + (\chi/\kappa)^2}}. \qquad (18)$$

The reason is just that for arm-and-longitudinal, the mean photon number reaches its maximum in the steady state (compare the full and dashed-dotted lines in Fig. 1).

For long times, $\kappa\tau \gg 1$, we obtain

$$\begin{aligned}
\mathrm{SNR}_{\mathrm{A\&L}} &\approx \sqrt{8}\frac{\alpha_{\mathrm{arm}}|\chi|}{\kappa}\sqrt{\kappa\tau} \\
&= \sqrt{8\bar{n}_{\max}}\frac{|\chi|/\kappa}{\sqrt{1 + \chi^2/\kappa^2}}\sqrt{\kappa\tau}, \qquad (19)
\end{aligned}$$

where in the second line we have used Eq. (18). This has the same long-time scaling with the measurement time as dispersive and arm-and-release readout. Fixing $\bar{n}_{\max}$ and the integration time, the SNR saturates at large $|\chi|/\kappa$.

V. COMPARISON OF THE READOUT APPROACHES

Let us now put into perspective the results and discussions of the previous three sections. We have introduced an extra level of time-dependent control to extend arm-and-release to arm-and-longitudinal readout. Both of these schemes have a short-time SNR that scales with time as the ideal longitudinal readout [28] and that offers an improvement over that of dispersive readout. For the opposite limit of long times, all three schemes have the same scaling with time. These two observations beg the questions of which one is the superior scheme and how much we gain with it. We will see that these questions do not have simple answers and, in fact, depending on the device parameters represented by the ratio $|\chi|/\kappa$ and the measurement time (see the examples given in Sec. I), either arm-and-release or arm-and-longitudinal is the best alternative.

Let us start this discussion with a close inspection of the phase-space trajectories of the three readout schemes. In Figs. 3(a)– 3(c), we show the trajectories for $\alpha_g(t)$—since $\alpha_e(t)$ is its mirror image—for the ratios $|\chi|/\kappa = 1/3$, 1, and 3. In all three panels, the full lines show the trajectories for arm-and-release for some illustrative values of α_{arm}, the black dashed line shows the trajectory of dispersive readout, and the red dashed line shows the trajectory of arm-and-longitudinal. Same-color dots on different trajectories represent the positions of the evolving amplitude at equal times ($\kappa t = 0, 1, 2, 4, 10$, and 20). Importantly, across all three panels and all trajectories, the maximum mean photon number that is attained is the same.

As can be observed, interestingly, when $|\chi|/\kappa$ is small, α_{arm} in arm-and-release can be used as a control parameter to interpolate between dispersive readout ($\alpha_{\mathrm{arm}} \to 0$) and arm-and-longitudinal ($\alpha_{\mathrm{arm}} \to \sqrt{n_{\max}}$). Note, however, that for arm-and-release, the constraint of a fixed maximum mean photon number implies that the drive amplitude depends on the value of the initial cavity amplitude, i.e., $\varepsilon_1 \to \varepsilon_1(\alpha_{\mathrm{arm}})$. To see this, consider a fixed value of the ratio $|\chi|/\kappa$. Then, as the value of α_{arm} is increased, the maximum mean photon number is reached at shorter and shorter times. As a consequence, the value of ε_1 decreases, thus effectively moving the steady-state fixed points α_g^s closer to the origin. This can be seen more markedly in Fig. 3(c) for $|\chi|/\kappa = 3$, indicating the existence of a trade-off between the speed of evolution at short times and the separation distance between the steady-state fixed points. As a result, for large values of $|\chi|/\kappa$, arm-and-release might not provide an advantage over dispersive readout, an observation that can be made precise by studying the SNR. Indeed, in the intermediate to long-time regime, the SNR is dominated by a term proportional to ε_1 [cf. Eq. (12)]; thus, having a ε_1 that decreases with increasing α_{arm} greatly diminishes the performance of the scheme.

In contrast, the horizontal trajectory of arm-and-longitudinal avoids this trade-off altogether. In fact, we are guaranteed to reach the maximum separation distance between the time-evolving amplitudes at steady state. As such, arm-and-longitudinal might be slower at short times than, say, arm-and-release for some values of α_{arm}, as can be appreciated from the equal time dots in Figs. 3(a)– 3(c). However, in the regime of intermediate to long times, the separation between the pointer states is larger for arm-and-longitudinal readout than the other two schemes, specially as $|\chi|/\kappa$ is increased. This yields a purely geometrical advantage for arm-and-longitudinal over the other two approaches.

It is also useful to consider the assignment (or single-shot) measurement error, defined as $E_m = (1/2)[P(e\,|\,g) + P(g\,|\,e)]$, where $P(n\,|\,m)$ is the probability of assigning the qubit to be in the state n when it is actually in m [41]. For the Gaussian distributions that we are considering, the assignment error is related to the SNR [3] by $E_m = (1/2)\mathrm{erfc}(\mathrm{SNR}/2)$, where erfc is the complementary error function. In Figs. 3(d)– 3(f), we plot the assignment error for each of the trajectories of Figs. 3(a)– 3(c). For $|\chi|/\kappa = 1/3$ in Fig. 3, the error of the arm-and-release scheme (solid lines) always improves over the error of dispersive readout (black dashed line) and at larger α_{arm}, it is always better. Upon increasing the value of $|\chi|/\kappa$, there is crossing of the curves corresponding to the different schemes. For short times, the largest α_{arm} results in the smallest error, yet for larger times its performance is the worst. This is in agreement with the geometric picture of the trajectories, which is most evident in Fig. 3(f), for $|\chi|/\kappa = 3$, where
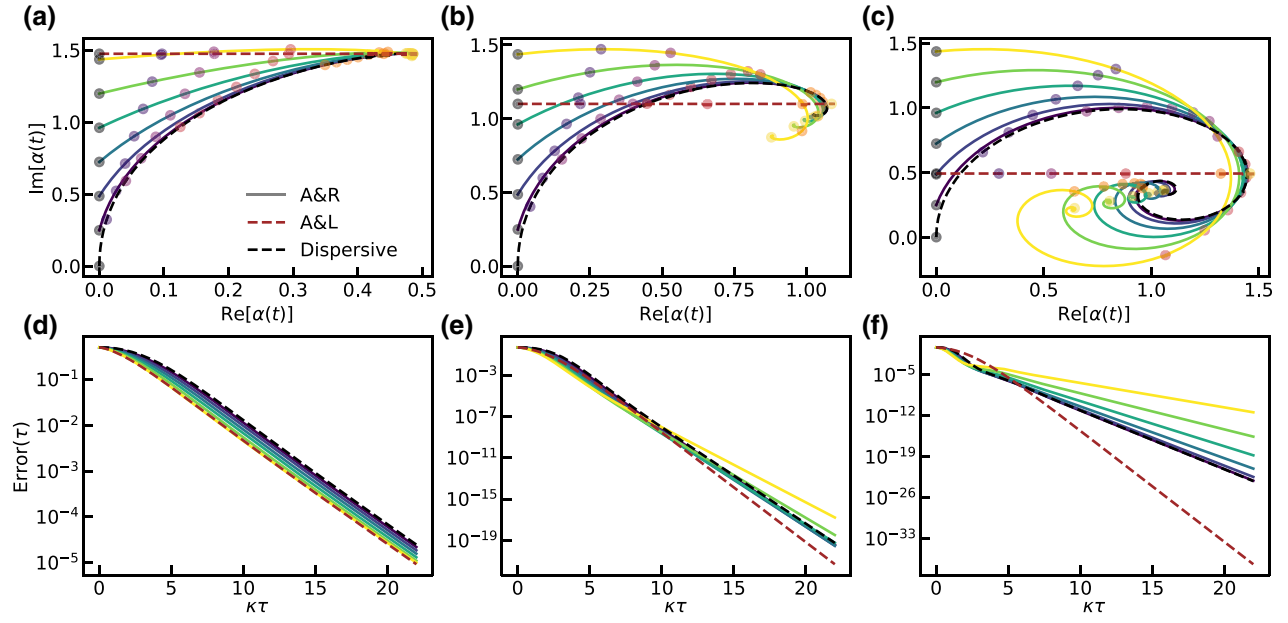
FIG. 3. (a)–(c) The path in phase space of the cavity amplitude $\alpha_g(t)$ for the three different schemes: (a) $|\chi|/\kappa = 1/3$; (b) $|\chi|/\kappa = 1$; (c) $|\chi|/\kappa = 3$. Key to lines: black dashed line, standard dispersive readout; full lines, arm-and-release; red dashed line, arm-and-longitudinal. The different colors for the arm-and-release trajectories indicate different initial amplitudes α_{arm}, while the colored dots indicate different times in the evolution, $\kappa t = 0, 1, 2, 4, 10$, and 20. All trajectories, in all three panels, visit the same maximum mean photon number $n_{\text{max}} = 2.44$. (d)–(f) The assignment error as a function of the measurement integration time for the corresponding trajectories depicted in (a)–(c). From left to right, the parameters are as follows: $|\chi|/\kappa = 1/3, 1$, and 3 and, for arm-and-longitudinal, $\alpha_{\text{arm}}/\sqrt{n_{\text{max}}} = \sqrt{9}/\sqrt{10}, 1/\sqrt{2}$, and $1/\sqrt{10}$. For dispersive readout, $\varepsilon_1/2\pi = 15.77$ MHz, 19.85 MHz, and 34.38 MHz. For arm-and-release, $\alpha_{\text{arm}} \in \left(0, \sqrt{n_{\text{max}}}\right]$ and ε_1 is obtained, after fixing α_{arm}, from the constraint of having less than the maximum mean photon number.

the largest arming amplitude gives the worst performance and, instead, arm-and-longitudinal readout yields a large improvement (note the change in the range of the vertical axis amongst Figs. 3(d)– 3(f)). This observation opens the door to achieving improved readout performance in parameter regimes far from the well-known optimal working point $|\chi|/\kappa = 1$ of dispersive readout.

A. Arm-and-release readout versus dispersive readout

Up to this point, we have presented qualitative and quantitative arguments in support of an improvement offered by arm-and-release readout over dispersive readout, noting that there may exist a region in the parameter space $(|\chi|/\kappa, \kappa\tau)$ where dispersive readout is the superior scheme. In this subsection, we quantify the extent of the improvement offered by arm-and-release as well as identifying the region in parameter space where this improvement is guaranteed.

To quantify the improvement offered by arm-and-release readout, we introduce the relative gain

$$\mathcal{G}_{\text{A\&R}}(\chi, \kappa, \tau) = \frac{\max\limits_{\alpha_{\text{arm}}} \{\text{SNR}_{\text{A\&R}}(\chi, \kappa, \tau, \alpha_{\text{arm}})\}}{\text{SNR}_{\text{disp}}(\chi, \kappa, \tau)}, \quad (20)$$

where $\text{SNR}_{\text{disp}}(\chi, \kappa, \tau) = \text{SNR}_{\text{A\&R}}(\chi, \kappa, \tau, \alpha_{\text{arm}} = 0)$. The maximization is taken considering the constraint that both methods should lead to the same maximum mean photon number. In Fig. 4(a), we show this relative gain as a function of the ratio $|\chi|/\kappa$ and the measurement time $\kappa\tau$. We observe a large region of this parameter space where arm-and-release is advantageous, reaching gains as large as $\mathcal{G}_{\text{A\&R}} \sim 400$ for $\kappa\tau \ll 1$ (not shown) and small $|\chi|/\kappa$, and $\mathcal{G}_{\text{A\&R}} \sim 2$ at intermediate times. However, this advantage decreases at large $|\chi|/\kappa$ and for readout times ranging from intermediate, $\kappa\tau \sim 4.5$, all the way to the asymptotic limit, where dispersive readout is advantageous. The gray region in Fig. 4(a) delimits the transition between the two regimes where one or the other scheme performs better. This is consistent with the geometrical argument for the trajectories discussed before, by which at intermediate to long times the coherent amplitudes are in close proximity to the steady-state fixed points and these are closer to the origin for arm-and-release when $|\chi|/\kappa$ is large.

In Fig. 4(b), we show the normalized value of the amplitude, $\tilde{\alpha}_{\text{arm}} = \alpha_{\text{arm}}^{\text{optimal}}/\sqrt{\bar{n}_{\text{max}}}$, that maximizes the relative gain $\mathcal{G}_{\text{A\&R}}$ of Fig. 4(a). The normalization bounds it to $\tilde{\alpha}_{\text{arm}} \in [0, 1]$, making it universal. Hence, the optimal value of α_{arm} for any system parameters can be deduced from
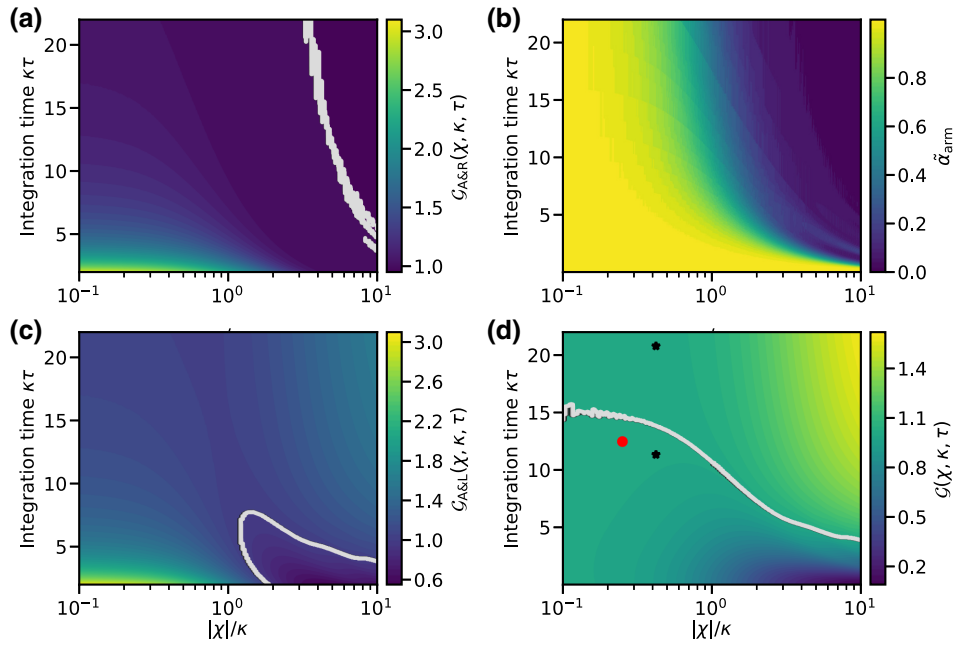
FIG. 4. (a) The SNR relative gain between arm-and-release and dispersive readout [see Eq. (20)], as a function of $|\chi|/\kappa$ and the measurement integration time. (b) The optimal value of the (normalized) amplitude $\tilde{\alpha}_{arm}$ associated with the best SNR in (a). (c) The SNR relative gain between arm-and-longitudinal and dispersive readout [see Eq. (21)], as a function of $|\chi|/\kappa$ and the measurement integration time. (d) The ratio between the relative gains of arm-and-longitudinal and arm-and-release [see Eq. (22)]. The black stars correspond to the parameters of the experiment in Ref. [9] and the red dot to those of Ref. [7] (in which arm-and-release was used; see the text). In (a), (c), and (d), the gray contours indicate the separation between the regions with different optimal-readout strategies. In all panels, for a given $|\chi|/\kappa$, all other parameters are fixed by the choice of n_{max}.

Fig. 4(b) by rescaling $\tilde{\alpha}_{arm}$ by the appropriate maximum mean photon number that is desired. The reasoning behind this is that all relative gains remain unchanged under the rescaling $\alpha_{arm} \rightarrow \alpha_{arm}/\sqrt{n}$ and $\varepsilon_1 \rightarrow \varepsilon_1/\sqrt{n}$, as this constitutes shrinking the whole phase space to the region at the interior of the unit circle. Figure 4(b) gives an interpretation to the region on the right of the gray contour in Fig. 4(a), where arm-and-release does not offer an advantage over dispersive readout. Since in this region $\tilde{\alpha}_{arm} \sim 1$, the maximum mean photon number of the phase-space paths occurs at times $\kappa\tau \rightarrow 0$, thus leading to fixed points $\alpha_{g,e}^s$ that are almost at the origin.

B. Arm-and-longitudinal readout versus dispersive readout

While there is a region of parameter space where dispersive readout is favorable with respect to arm-and-release [cf. Fig. 4(a)], we now show that arm-and-longitudinal offers a large improvement over arm-and-release in that region. To quantify this, we introduce the relative gain of arm-and-longitudinal as

$$\mathcal{G}_{A\&L}(\chi, \kappa, \tau) = \frac{SNR_{A\&L}(\chi, \kappa, \tau, \alpha_{arm})}{SNR_{disp}(\chi, \kappa, \tau)}. \quad (21)$$

In Fig. 4(c), we show this relative gain in the parameter space $(|\chi|/\kappa, \kappa\tau)$. The arm-and-longitudinal readout scheme offers a large gain $\mathcal{G}_{A\&L} \sim 400$ at $\kappa\tau \ll 1$ (not shown), similar to the relative gain of arm-and-release, a consequence of the finite armed photons. Overall, arm-and-longitudinal performs better than dispersive readout, except in the region of large $|\chi|/\kappa$ and short measurement times, which is delimited by the gray contour in Fig. 4(c). In particular, in the region where the advantage of arm-and-release over dispersive readout was not guaranteed, now arm-and-longitudinal is the best of the three methods [compare Figs. 4(a) and 4(c)]. In short, qubit cloaking always allows us to improve the readout fidelity regardless of the value of $|\chi|/\kappa$ and the measurement integration time.

We stress that even a modest gain $\mathcal{G}_{A\&L} \sim 2$ will yield a large improvement for the measurement discrimination error. This is illustrated in Fig. 3, which shows the assignment error E_m for $|\chi|/\kappa = 3$, where arm-and-longitudinal gives an improvement of several orders of magnitude at intermediate to long times. In fact, for a large SNR, $E_m = (1/2)erfc(SNR/2) \approx e^{-SNR^2/4}/(\sqrt{\pi}SNR)$, which means that a larger prefactor in the long-time scaling of the SNR can have a huge impact in the reduction of the error.

C. Arm-and-release versus arm-and-longitudinal: Which one should you use?

The results of the previous two subsections are summarized in Fig. 4(d), where we show the ratio

$$\mathcal{G}(\chi, \kappa, \tau) = \frac{\mathcal{G}_{A\&L}(\chi, \kappa, \tau)}{\mathcal{G}_{A\&R}(\chi, \kappa \tau)}$$

$$= \frac{\text{SNR}_{A\&L}(\chi, \kappa, \tau, \alpha_{arm})}{\max\limits_{\alpha_{arm}} \{\text{SNR}_{A\&R}(\chi, \kappa, \tau, \alpha_{arm})\}} \quad (22)$$

between the SNRs of arm-and-longitudinal and arm-and-release. Together, these two schemes always provide a better strategy than standard dispersive readout on current superconducting circuit experiments. All that is left is thus for us to make the recommendation of how, given the device parameters $|\chi|/\kappa$ and a target measurement integration time, to make the more out of this pair of schemes. The gray contour in Fig. 4(d) indicates $\mathcal{G}(\chi, \kappa, \tau) = 1$, separating the region where arm-and-longitudinal or arm-and-release is more advantageous. In the case where arm-and-release is the preferable choice, one can resort to Fig. 4(b) to identify the appropriate arming amplitude yielding the maximum improvement.

As an example, the experiment of Ref. [9] has performed readout of a transmon qubit with $|\chi|/\kappa = 0.42$ in $\kappa\tau = 11.31$ and 20.73 with 98.25% and 99.2% average fidelity, respectively. In Fig. 4(d), we show these two configurations (black stars), with our recommendation being arm-and-release and arm-and-longitudinal, respectively. We also indicate with a red dot the parameters of the *qubit cloaking* experiment in which arm-and-release has been used [7]. In all cases, the expected gain on SNR over dispersive readout is in the 20–30% range. Albeit modest, it can signify a large improvement in the discrimination error and thus the readout fidelity, as mentioned in the discussion of Figs. 3(d)– 3(f). Depending on the value of the SNR, the error can be reduced by up to 8%.

VI. FULL SYSTEM DYNAMICS

To simplify the presentation, the above discussion relies on the following three approximations: (i) truncation of the multilevel nonlinear system to a two-level system, (ii) the rotating-wave approximation, and (iii) the dispersive approximation. We now show that the readout trajectories can be made longitudinal-like even without using these approximations. As a concrete example, we consider a transmon qubit [42] coupled capacitively to a cavity with the Hamiltonian ($\hbar = 1$)

$$\hat{H}_0 = \omega_r \hat{a}^\dagger \hat{a} + 4E_C \hat{n}_{tr}^2 - E_J \cos(\hat{\varphi}_{tr}) + ig\hat{n}_{tr}(\hat{a}^\dagger - \hat{a}). \quad (23)$$
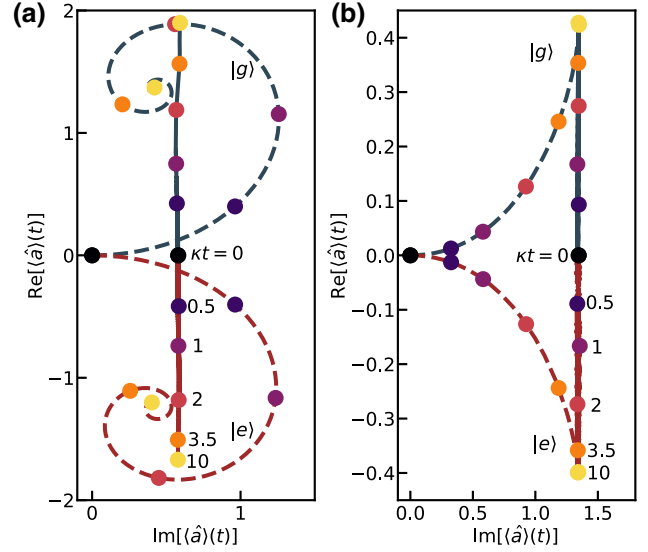

FIG. 5. Numerically obtained paths of the cavity-pointer states in phase space using a transmon multilevel Hamiltonian, no RWA, and no dispersive approximation for arm-and-longitudinal (full lines) and standard dispersive readout (dashed lines). In (a) [(b)], we use $\kappa/2\pi = 1$ MHz (10.1 MHz), and for arm-and-longitudinal readout we choose $n_{tar} = 2$ (1), which is in between zero photons and the maximum number attained $\bar{n}_{max} = 4$ (2). This results in $|\chi_{n_{tar}}|/\kappa = 3.286$ in (a) and 0.326 in (b). For the standard-dispersive-readout case, we use $\omega_1/2\pi = 7.665$ GHz (7.666 GHz) and $\varepsilon_1/2\pi = 4.876$ MHz (15 MHz) for (a) [(b)]. All the other system parameters read as follows: $E_J/2\pi = 16.93$ GHz, $E_C/2\pi = 200.4$ MHz, $g/2\pi = 159.1$ MHz, and $\omega_r/2\pi = 7.655$ GHz.

In this expression, $\hat{n}_{tr}$ and $\hat{\varphi}_{tr}$ are the transmon charge and phase operators, and E_C, E_J, and g are the charging, Josephson, and coupling frequencies, respectively [3]. To this Hamiltonian, we add the cavity drive term $\hat{H}_1(t) = i\varepsilon_1(t)\sin(\omega_1 t)(\hat{a}^\dagger - \hat{a})$ and we solve numerically the Lindblad equation

$$\partial_t \hat{\rho} = -i[\hat{H}_0 + \hat{H}_1(t), \hat{\rho}] + \kappa \mathcal{D}[\hat{a}](\hat{\rho}). \quad (24)$$

We modulate $\varepsilon_1(t)$ as in Eq. (13). Given that the arming time does not factor into the readout time, we begin our simulation for arm-and-longitudinal, shown in Fig. 5(b), with a preloaded cavity, and simulate the readout dynamics following the release of the cloaking mechanism.

In Fig. 5, we show the numerically obtained readout phase-space trajectories for arm-and-longitudinal (full lines) and standard dispersive readout (dashed lines) for two values of the ratio $|\chi_{n_{tar}}|/\kappa \approx 3.3$ [Fig. 5(a)] and $|\chi_{n_{tar}}|/\kappa \approx 0.3$ [Fig. 5(b)]. Here, $\chi_{n_{tar}}$ is the numerically obtained dispersive shift evaluated at a target photon number n_{tar} (for details, see Appendix C). The colored dots correspond to times $t = 0$, 0.5, 1, 2, 3.5, and 10, in units of $1/\kappa$. This figure shows that even when using

the full transmon Hamiltonian and not using the rotating-wave or dispersive approximations, the readout trajectories can be made longitudinal-like via the modulation of the drive amplitude, as in Eq. (13). Moreover, in agreement with Figs. 3 and 4, the best improvement of arm-and-longitudinal over standard dispersive readout is obtained for long times when $|\chi|/\kappa > 1$, as is evident here from the much larger separation of the average cavity amplitudes for arm-and-longitudinal readout in Fig. 5(a) [note the change in vertical scale between Figs. 5(a) and 5(b)]. The only system parameter that we change in Figs. 5(a) and 5(b) is $\kappa/2\pi$, taking values 1 MHz and 10.1 MHz, respectively. We note that the asymmetry observed between the ground- and excited-state paths in phase space is due to Purcell decay, which affects both dispersive and arm-and-longitudinal readout in similar ways. As discussed in Ref. [7], qubit cloaking and thus arm-and-longitudinal works with minimal change in the presence of a Purcell filter.

VII. DISCUSSION AND OUTLOOK

We have studied the arm-and-release and arm-and-longitudinal readout schemes, which are derived from qubit cloaking [7]. Both are a direct consequence of our ability to prearm the cavity with photons in anticipation of the readout dynamics. These two approaches complement each other and together offer a modest advantage over standard dispersive readout for all values of the ratio $|\chi|/\kappa$ and measurement times. Since qubit cloaking relies on standard circuit-QED hardware [7], this advantage can be achieved free of hardware overhead, i.e., no alteration to this architecture is required. Arm-and-longitudinal is realized by a slow turn-off of the cavity readout drive. The resulting control over the cavity mean photon population makes this scheme suitable for preventing undesirable measurement-induced transitions and qubit ionization. We thus hope that our results will help current and future circuit-QED experiments to perform readout at or close to the state-of-the-art level while relaxing some parameter optimizations.

An interesting future avenue of research that might yield improved readout schemes is to exploit the complementarity of the two schemes discussed in this work. The combination of rapid evolution under arm-and-release for short times, $\kappa\tau \sim 2$, followed by time modulation of the drive amplitude, could bring together the best of both schemes. This hybrid strategy is guaranteed to succeed provided that $\mathrm{Im}[\alpha_g(t_0)] = \mathrm{Im}[\alpha_e(t_0)]$ is treated as a new initial condition for the dynamical problem [cf. the discussion around Eq. (13)].

The longitudinal phase-space evolution of the cavity amplitude during arm-and-longitudinal may also be useful beyond the task of qubit readout. For instance, the error-correction cycles with the GKP code use phase-space motions of the cavity amplitude that are quasilongitudinal [43,44]: it is interesting to explore the extent to which these error-correction schemes might see an improvement using the protocol presented in this work. Furthermore, the longitudinal phase-space motion could also be useful in implementing cavity-assisted two-qubit gates that rely on the geometric phase of the cavity field [45].

APPENDIX A: MEAN PHOTON NUMBER AND SIGNAL-TO-NOISE RATIO FOR ARM-AND-RELEASE READOUT

In this appendix, we present the expressions for the time dependence of the mean photon number and the SNR for the arm-and-release scheme, as well as for standard dispersive readout, which is recovered in the limit $\alpha_{\mathrm{arm}} \to 0$. The mean photon number is directly computed from Eq. (7) as $\bar{n}(t) = |\alpha(t)|^2$ and we obtain

$$\bar{n}_{\mathrm{A\&R}}(t) = \frac{\varepsilon_1^2}{\chi^2 + \kappa^2}(1 + e^{-\frac{\kappa}{2}t}) + \alpha_{\mathrm{arm}}^2 e^{-\kappa t}$$
$$+ \frac{\varepsilon_1}{\chi^2 + \kappa^2}\left[2\alpha_{\mathrm{arm}}\left[\chi\sin\left(\frac{\chi}{2}t\right) + \kappa\cos\left(\frac{\chi}{2}t\right) - \kappa e^{-\frac{\kappa}{2}t}\right] - 2\varepsilon_1\cos\left(\frac{\chi}{2}t\right)\right]e^{-\kappa t/2}. \quad (A1)$$

The SNR is computed directly from Eq. (9). We find that

$$
\begin{aligned}
\frac{\mathrm{SNR}^2_{\mathrm{A\&R}}}{8\kappa} &= \frac{\varepsilon_1^2 \chi^2}{(\kappa^2 + \chi^2)^2}\tau - \frac{4\varepsilon_1^2 \chi^2}{(\chi^2 + \kappa^2)^3}\left[\kappa - \left(\kappa \cos\left(\frac{\chi}{2}\tau\right) - \chi \sin\left(\frac{\chi}{2}\tau\right)\right)e^{-\frac{\kappa}{2}\tau}\right] \\
&+ \frac{\varepsilon_1^2 \chi^2}{2\kappa(\chi^2 + \kappa^2)^3}\left[\chi^2 + 2\kappa^2 - \left(\chi^2 + \kappa^2 + \kappa^2\cos(\chi\tau) - \chi\kappa\sin(\chi\tau)\right)e^{-\kappa\tau}\right] \\
&- \frac{4\varepsilon_1^2 \kappa \chi}{(\chi^2 + \kappa^2)^3}\left[\chi - \left(\cos\left(\frac{\chi}{2}\tau\right) + \kappa\sin\left(\frac{\kappa}{2}\tau\right)\right)e^{-\frac{\kappa}{2}\tau}\right] \\
&+ \frac{\varepsilon_1^2 \kappa \chi}{(\chi^2 + \kappa^2)^3}\left[\chi - (\chi\cos(\chi\tau) + \kappa\sin(\chi\tau))e^{-\kappa\tau}\right] \\
&+ \frac{\varepsilon_1^2 \kappa}{2(\chi^2 + \kappa^2)^3}\left[\chi^2 - (\chi^2 + \kappa^2 - \kappa^2\cos(\chi\tau) + \kappa\chi\sin(\chi\tau))e^{-\kappa\tau}\right] \\
&+ \frac{4\alpha_{\mathrm{arm}}\varepsilon_1 \chi}{(\chi^2 + \kappa^2)^2}\left[\chi - \left(\chi\cos\left(\frac{\chi}{2}\tau\right) + \kappa\sin\left(\frac{\chi}{2}\tau\right)\right)e^{-\frac{\kappa}{2}\tau}\right] \\
&- \frac{\alpha_{\mathrm{arm}}\varepsilon_1 \chi}{(\chi^2 + \kappa^2)^2}\left[\chi - (\chi\cos(\chi\tau) + \kappa\sin(\chi\tau))e^{-\kappa\tau}\right] \\
&+ \frac{\alpha_{\mathrm{arm}}^2}{2\kappa(\chi^2 + \kappa^2)}\left[\chi^2 - \left(\chi^2 + \kappa^2 - \kappa^2\cos(\chi\tau) + \kappa\chi\sin(\chi\tau)\right)e^{-\kappa\tau}\right] \\
&- \frac{\alpha_{\mathrm{arm}}\varepsilon_1}{(\chi^2 + \kappa^2)^2}\left[\chi^2 - \left(\chi^2 + \kappa^2 - \kappa^2\cos(\chi\tau) + \kappa\chi\sin(\chi\tau)\right)e^{-\kappa\tau}\right].
\end{aligned}
\tag{A2}
$$

APPENDIX B: EXPLICIT FORM OF THE DRIVE AMPLITUDE FOR ARM-AND-LONGITUDINAL READOUT

As mentioned in Sec. IV, our starting point is the equation of motion for the intracavity-field amplitude with a resonant drive, $\omega_1 = \omega_r$, given by

$$
\dot{\alpha}_{g,e} = -(\mp i\chi/2 + \kappa/2)\alpha_{g,e} + i\varepsilon_1(t)/2, \tag{B1}
$$

and its formal solution,

$$
\alpha_e(t) = \alpha(0)e^{-(i\frac{\chi}{2} + \frac{\kappa}{2})t} + \frac{i}{2}\int_0^t e^{-(i\frac{\chi}{2} + \frac{\kappa}{2})(t-t')}\epsilon(t')dt', \tag{B2}
$$

where $\alpha_g(t) = \alpha_e(t; \chi \to -\chi)$. Furthermore, given that our initial condition is $\mathrm{Re}[\alpha(0)] = 0$ and $\mathrm{Im}[\alpha(0)] = \alpha_{\mathrm{arm}}$, where α_{arm} is a positive real number, we achieve our goal of making the trajectories separate along the X quadrature if the condition $\mathrm{Im}[\alpha_{g,e}(t)] = \alpha_{\mathrm{arm}}$ is satisfied for all times $t \geq 0$. This immediately implies $d/dt\mathrm{Im}[\alpha(t)] = 0$ and after plugging this into Eq. (B1), we obtain

$$
\epsilon_1(t) = \chi\mathrm{Re}[\alpha(t)] + \kappa\mathrm{Im}[\alpha(t)], \tag{B3}
$$

where we have dropped the sign dependence on χ, as this will not affect the final outcome, which is qubit-state independent.

At this point, we split Eq. (B2) into its real and imaginary parts, and plug them into Eq. (B3) to obtain

$$
\varepsilon_1(t) = 2\alpha_{\mathrm{arm}}K(t, 0) + \int_0^t d\tau K(t, \tau)\varepsilon_1(\tau), \tag{B4}
$$

where the kernel reads

$$
\begin{aligned}
K(t, \tau) &= \frac{1}{2}\left[\chi\sin\left(\frac{\chi}{2}(t - \tau)\right) + \kappa\cos\left(\frac{\chi}{2}(t - \tau)\right)\right] \\
&\times e^{-\frac{\kappa}{2}(t-\tau)}.
\end{aligned}
\tag{B5}
$$

The expression in Eq. (B4) is a Volterra integral equation of the second kind (see Ref. [46, Chap. 16]). Importantly, this kernel is separable, meaning that it can be written as

$$
K(t, \tau) = \sum_{l=1}^{L} G_l(t)W_l(\tau), \tag{B6}
$$

for some integer L and some functions $\{G_l\}$ and $\{W_l\}$. This fact is a sufficient condition for the integral equation to have a unique solution (see Ref. [46, Chap. 16]). This solution reads

$$
\epsilon_1(t) = \frac{\alpha_{\mathrm{arm}}\chi^2}{\kappa}\left(1 - e^{-\frac{\kappa}{2}t}\right) + \alpha_{\mathrm{arm}}\kappa, \tag{B7}
$$

given in Eq. (13).

APPENDIX C: NUMERICAL DETERMINATION OF χ FOR THE FULL-COSINE TRANSMON MODEL

With the approximations introduced in Sec. II, the dispersive interaction takes the usual form of approximately $\chi\hat{\sigma}^{+}\hat{\sigma}^{-}\hat{a}^{\dagger}\hat{a}$, where the dispersive shift χ is independent of the photon number. Here, for a multilevel system, using perturbation theory to approximately diagonalize the system Hamiltonian gives

$$\hat{U}^{\dagger}\hat{H}_0\hat{U} \approx \tilde{\omega}_r\hat{a}^{\dagger}\hat{a} + \sum_i \tilde{\epsilon}_i \ket{i}\bra{i} + \sum_{i,n} n\chi_{i,n}\ket{i,n}\bra{i,n},$$

(C1)

where $\tilde{\omega}_r$ is the Lamb-shifted cavity frequency and the dispersive interaction $\chi_{i,n}$ now depends on the cavity Fock number n [3]. Here, $\{\tilde{\epsilon}_i\}$ and $\{\ket{i}\}$ with $i = g, e, f, \dots$ correspond, respectively, to the Lamb-shifted energies and the eigenstates of the transmon Hamiltonian $4E_C\hat{n}_{\mathrm{tr}} - E_J\cos(\hat{\varphi}_{\mathrm{tr}})$. The actual eigenstates of $\hat{H}_0$, labeled $\ket{\overline{i,n}} = \hat{U}\ket{i,n}$, have associated eigenvalues $\epsilon_{\overline{i,n}} \approx (\tilde{\omega}_r + \chi_{i,n})n + \tilde{\epsilon}_i$ according to Eq. (C1). We can define energy branches for each of the transmon states (see Ref. [22]). The branch associated with the transmon being in the ground (excited) state corresponds approximately to cavity energies $(\tilde{\omega}_r + \chi_{g(e),n})n$. Choosing an optimal drive frequency for readout with a target Fock number n_{tar} corresponds to using $\omega_1 = \tilde{\omega}_r + (\chi_{g,n_{\mathrm{tar}}} + \chi_{e,n_{\mathrm{tar}}})/2$, exactly in between the two branches at that Fock number. The full dispersive shift at n_{tar} is given by $\chi_{n_{\mathrm{tar}}} \equiv \chi_{e,n_{\mathrm{tar}}} - \chi_{g,n_{\mathrm{tar}}}$. In the modulation of the drive amplitude [see Eq. (13)], instead of χ, we use $\chi_{n_{\mathrm{tar}}}$ with a chosen n_{tar}. Our protocol works perfectly well as long as χ_n does not change dramatically from the initial $n \sim \bar{n} = |\alpha_{\mathrm{arm}}|^2$ mean photon number to the steady-state $n \sim \bar{n}^s = n_{\max}$ maximum mean photon number. In particular, the dynamics should not lead to photon numbers that are so large that transitions to higher transmon energy levels ($i = f, \dots$) are induced [4,8,21–23].

---

[1] M. A. Nielsen and I. L. Chuang, *Quantum Computation and Quantum Information: 10th Anniversary Edition* (Cambridge University Press, New York, 2010).

[2] A. Blais, R.-S. Huang, A. Wallraff, S. M. Girvin, and R. J. Schoelkopf, Cavity quantum electrodynamics for superconducting electrical circuits: An architecture for quantum computation, Phys. Rev. A **69**, 062320 (2004).

[3] A. Blais, A. L. Grimsmo, S. M. Girvin, and A. Wallraff, Circuit quantum electrodynamics, Rev. Mod. Phys. **93**, 025005 (2021).

[4] D. Sank, *et al.*, Measurement-induced state transitions in a superconducting qubit: Beyond the rotating wave approximation, Phys. Rev. Lett. **117**, 190503 (2016).

[5] C. C. Bultink, M. A. Rol, T. E. O'Brien, X. Fu, B. C. S. Dikken, C. Dickel, R. F. L. Vermeulen, J. C. de Sterke, A. Bruno, R. N. Schouten, and L. DiCarlo, Active resonator reset in the nonlinear dispersive regime of circuit QED, Phys. Rev. Appl. **6**, 034008 (2016).

[6] S. Touzard, A. Kou, N. E. Frattini, V. V. Sivak, S. Puri, A. Grimm, L. Frunzio, S. Shankar, and M. H. Devoret, Gated conditional displacement readout of superconducting qubits, Phys. Rev. Lett. **122**, 080502 (2019).

[7] C. Lledó, R. Dassonneville, A. Moulinas *et al.*, Cloaking a qubit in a cavity, Nat. Commun. **14**, 6313 (2023).

[8] M. Khezri, A. Opremcak, Z. Chen, A. Bengtsson, T. White, O. Naaman, R. Acharya, K. Anderson, M. Ansmann, and F. Arute, *et al.*, Measurement-induced state transitions in a superconducting qubit: Within the rotating wave approximation, ArXiv:2212.05097 (2022).

[9] T. Walter, P. Kurpiers, S. Gasparinetti, P. Magnard, A. Potočnik, Y. Salathé, M. Pechal, M. Mondal, M. Oppliger, C. Eichler, and A. Wallraff, Rapid high-fidelity single-shot dispersive readout of superconducting qubits, Phys. Rev. Appl. **7**, 054020 (2017).

[10] Y. Sunada, S. Kono, J. Ilves, S. Tamate, T. Sugiyama, Y. Tabuchi, and Y. Nakamura, Fast readout and reset of a superconducting qubit coupled to a resonator with an intrinsic Purcell filter, Phys. Rev. Appl. **17**, 044016 (2022).

[11] L. Chen, *et al.*, Transmon qubit readout fidelity at the threshold for quantum error correction without a quantum-limited amplifier, npj Quantum Inf. **9**, 26 (2023).

[12] R. Dassonneville, T. Ramos, V. Milchakov, L. Planat, E. Dumur, F. Foroughi, J. Puertas, S. Leger, K. Bharadwaj, J. Delaforce, C. Naud, W. Hasch-Guichard, J. J. García-Ripoll, N. Roch, and O. Buisson, Fast high-fidelity quantum nondemolition qubit readout via a nonperturbative cross-Kerr coupling, Phys. Rev. X **10**, 011045 (2020).

[13] V. Negîrneac, H. Ali, N. Muthusubramanian, F. Battistel, R. Sagastizabal, M. S. Moreira, J. F. Marques, W. J. Vlothuizen, M. Beekman, C. Zachariadis, N. Haider, A. Bruno, and L. DiCarlo, High-fidelity controlled-Z gate with maximal intermediate leakage operating at the speed limit in a superconducting quantum processor, Phys. Rev. Lett. **126**, 220502 (2021).

[14] Q. Ficheux, L. B. Nguyen, A. Somoroff, H. Xiong, K. N. Nesterov, M. G. Vavilov, and V. E. Manucharyan, Fast logic with slow qubits: Microwave-activated controlled-Z gate on low-frequency fluxoniums, Phys. Rev. X **11**, 021026 (2021).

[15] Y. Xu, J. Chu, J. Yuan, J. Qiu, Y. Zhou, L. Zhang, X. Tan, Y. Yu, S. Liu, J. Li, F. Yan, and D. Yu, High-fidelity, high-scalability two-qubit gate scheme for superconducting qubits, Phys. Rev. Lett. **125**, 240503 (2020).

[16] L. Ding, M. Hays, Y. Sung, B. Kannan, J. An, A. D. Paolo, A. H. Karamlou, T. M. Hazard, K. Azar, D. K. Kim, B. M. Niedzielski, A. Melville, M. E. Schwartz, J. L. Yoder, T. P. Orlando, S. Gustavsson, J. A. Grover, K. Serniak, and W. D. Oliver, High-fidelity, frequency-flexible two-qubit fluxonium gates with a transmon coupler, ArXiv:2304.06087 (2023).

[17] C. K. Andersen, A. Remm, S. Lazar, S. Krinner, N. Lacroix, G. J. Norris, M. Gabureac, C. Eichler, and A. Wallraff, Repeated quantum error detection in a surface code, Nat. Phys. **16**, 875 (2020).

[18] S. Krinner, N. Lacroix, A. Remm, A. Di Paolo, E. Genois, C. Leroux, C. Hellings, S. Lazar, F. Swiadek, and J.

Herrmann, *et al.*, Realizing repeated quantum error correction in a distance-three surface code, Nature **605**, 669 (2022).

[19] R. Acharya, *et al.*, Suppressing quantum errors by scaling a surface code logical qubit, Nature **614**, 676 (2023).

[20] Y. Zhao, *et al.*, Realization of an error-correcting surface code with superconducting qubits, Phys. Rev. Lett. **129**, 030501 (2022).

[21] R. Lescanne, L. Verney, Q. Ficheux, M. H. Devoret, B. Huard, M. Mirrahimi, and Z. Leghtas, Escape of a driven quantum Josephson circuit into unconfined states, Phys. Rev. Appl. **11**, 014030 (2019).

[22] R. Shillito, A. Petrescu, J. Cohen, J. Beall, M. Hauru, M. Ganahl, A. G. Lewis, G. Vidal, and A. Blais, Dynamics of transmon ionization, Phys. Rev. Appl. **18**, 034031 (2022).

[23] J. Cohen, A. Petrescu, R. Shillito, and A. Blais, Reminiscence of classical chaos in driven transmons, PRX Quantum **4**, 020312 (2023).

[24] D. I. Schuster, A. Wallraff, A. Blais, L. Frunzio, R.-S. Huang, J. Majer, S. M. Girvin, and R. J. Schoelkopf, ac Stark shift and dephasing of a superconducting qubit strongly coupled to a cavity field, Phys. Rev. Lett. **94**, 123602 (2005).

[25] M. Boissonneault, J. M. Gambetta, and A. Blais, Dispersive regime of circuit QED: Photon-dependent qubit dephasing and relaxation rates, Phys. Rev. A **79**, 013819 (2009).

[26] A. Petrescu, M. Malekakhlagh, and H. E. Türeci, Lifetime renormalization of driven weakly anharmonic superconducting qubits. II. The readout problem, Phys. Rev. B **101**, 134510 (2020).

[27] M. Malekakhlagh, A. Petrescu, and H. E. Türeci, Lifetime renormalization of weakly anharmonic superconducting qubits. I. Role of number nonconserving terms, Phys. Rev. B **101**, 134509 (2020).

[28] N. Didier, J. Bourassa, and A. Blais, Fast quantum nondemolition readout by parametric modulation of longitudinal qubit-oscillator interaction, Phys. Rev. Lett. **115**, 203601 (2015).

[29] T. Roy, S. Kundu, M. Chand, S. Hazra, N. Nehra, R. Cosmic, A. Ranadive, M. P. Patankar, K. Damle, and R. Vijay, Implementation of pairwise longitudinal coupling in a three-qubit superconducting circuit, Phys. Rev. Appl. **7**, 054025 (2017).

[30] C. Eichler and J. R. Petta, Realizing a circuit analog of an optomechanical system with longitudinally coupled superconducting resonators, Phys. Rev. Lett. **120**, 227702 (2018).

[31] J. Ikonen, J. Goetz, J. Ilves, A. Keränen, A. M. Gunyho, M. Partanen, K. Y. Tan, D. Hazra, L. Grönberg, V. Vesterinen, S. Simbierowicz, J. Hassel, and M. Möttönen, Qubit measurement by multichannel driving, Phys. Rev. Lett. **122**, 080503 (2019).

[32] H. Carmichael, *An Open Systems Approach to Quantum Optics: Lectures Presented at the Université Libre de Bruxelles, October 28 to November 4, 1991*, Lecture Notes in Physics Monographs (Springer-Verlag, Berlin, 2009).

[33] H.-P. Breuer and F. Petruccione, *The Theory of Open Quantum Systems* (Oxford University Press, Oxford, 2007).

[34] C. C. Bultink, B. Tarasinski, N. Haandbæk, S. Poletto, N. Haider, D. J. Michalak, A. Bruno, and L. DiCarlo, General method for extracting the quantum efficiency of dispersive qubit readout in circuit QED, Appl. Phys. Lett. **112**, 092601 (2018).

[35] C. Gardiner and P. Zoller, *Quantum Noise: A Handbook of Markovian and Non-Markovian Quantum Stochastic Methods with Applications to Quantum Optics*, Springer Series in Synergetics (Springer, Berlin, 2000).

[36] J. Gambetta, W. A. Braff, A. Wallraff, S. M. Girvin, and R. J. Schoelkopf, Protocols for optimal readout of qubits using a continuous quantum nondemolition measurement, Phys. Rev. A **76**, 012325 (2007).

[37] We note that for a fixed drive amplitude, a large $|\chi|/\kappa$ ratio, and long measurement integration times, the optimal driving frequency for dispersive readout becomes $\omega_1 = \omega_r \pm (1/2)\sqrt{\chi^2 - \kappa^2}$. If, however, we fix the maximum number of photons during readout, $\omega_1 = \omega_r$ is always the optimal driving frequency and the optimal value of $|\chi|/\kappa$ tends toward one as the integration time grows.

[38] Following Ref. [28], under a longitudinal interaction the cavity amplitude evolves as $\alpha_{g,e}(t) = \mp \tilde{g}_z/\kappa \left(1 - e^{-\kappa t/2}\right)$; thus we can readily integrate Eq. (9) and obtain $\mathrm{SNR}^2 = 8\tilde{g}_z^2/\kappa^2 \left(\kappa\tau - 3 + 4e^{-\kappa\tau/2} - e^{-\kappa\tau}\right)$.

[39] S. Richer and D. DiVincenzo, Circuit design implementing longitudinal coupling: A scalable scheme for superconducting qubits, Phys. Rev. B **93**, 134501 (2016).

[40] P.-M. Billangeon, J. S. Tsai, and Y. Nakamura, Circuit-QED-based scalable architectures for quantum information processing with superconducting qubits, Phys. Rev. B **91**, 094517 (2015).

[41] E. Magesan, J. M. Gambetta, A. D. Córcoles, and J. M. Chow, Machine learning for discriminating quantum measurement trajectories and improving readout, Phys. Rev. Lett. **114**, 200501 (2015).

[42] J. Koch, T. M. Yu, J. Gambetta, A. A. Houck, D. I. Schuster, J. Majer, A. Blais, M. H. Devoret, S. M. Girvin, and R. J. Schoelkopf, Charge-insensitive qubit design derived from the Cooper pair box, Phys. Rev. A **76**, eid 042319 (2007).

[43] A. Eickbusch, V. Sivak, A. Z. Ding, S. S. Elder, S. R. Jha, J. Venkatraman, B. Royer, S. Girvin, R. J. Schoelkopf, and M. H. Devoret, Fast universal control of an oscillator with weak dispersive coupling to a qubit, Nat. Phys. **18**, 1464 (2022).

[44] V. Sivak, A. Eickbusch, B. Royer, S. Singh, I. Tsioutsios, S. Ganjam, A. Miano, B. Brock, A. Ding, and L. Frunzio, *et al.*, Real-time quantum error correction beyond break-even, Nature **616**, 50 (2023).

[45] H. Paik, A. Mezzacapo, M. Sandberg, D. T. McClure, B. Abdo, A. D. Córcoles, O. Dial, D. F. Bogorin, B. L. T. Plourde, M. Steffen, A. W. Cross, J. M. Gambetta, and J. M. Chow, Experimental demonstration of a resonator-induced phase gate in a multiqubit circuit-QED system, Phys. Rev. Lett. **117**, 250502 (2016).

[46] G. B. Arfken and H. J. Weber, in *Mathematical Methods for Physicists* (Elsevier Academic Press, New York, 2005), 6th ed.